CHAPTER 6

A Review of the Application of Atomic Force Microscopy (AFM) in Food Science and Technology

Shaoyang Liu and **Yifen Wang**[1]

Contents

Abstract

Atomic force microscopy (AFM) is a powerful nanoscale analysis technique used in food area. This versatile technique can be used to acquire high-resolution sample images and investigate local interactions in air or liquid surroundings. In this chapter, we explain the principles of AFM and review representative applications of AFM in gelatin, casein micelle, carrageenan, gellan gum, starch, and interface. We elucidate new knowledge revealed with AFM as well as ways to use AFM to obtain morphology and rheology information in different food fields.

Biosystems Engineering Department, Auburn University, Auburn, Alabama, USA
[1] Corresponding author: Yifen Wang, *E-mail address:* wangyif@auburn.edu

Advances in Food and Nutrition Research, Volume 62
ISSN 1043-4526, DOI: 10.1016/B978-0-12-385989-1.00006-5

I. INTRODUCTION

Atomic force microscope (AFM) is a scanning near-field tool for nanoscale investigation which was invented in 1986 (Binnig *et al.*, 1986). Instead of using light or electron beam, AFM uses a sharp tip to ''feel'' samples. As the tip radius of curvature is on the order of nanometers, AFM can detect changes at a spatial resolution up to subnanometer level. Compared with other forms of microscopes, AFM has some unique features and special advantages. The optical microscope is a convenient tool for observation of samples at the microscale, but its resolution is limited by the wavelength of the light source to a maximum resolution of ca. 250 nm. Compared to the optical microscope, AFM has a much higher spatial resolution which provides the ability to investigate ultrafine structure of samples and even map the distribution of single molecules (Dufrene, 2008a; Engel and Muller, 2000). Scanning electron microscopy (SEM) and transmission electron microscopy (TEM) can also provide high resolution, but their complex sample preparation (e.g., chemical fixing, dehydration, metal coating, and ultrathin section) could distort the sample substantially. As AFM utilizes direct contact between the tip and the sample, minimum or even no sample preparation is required. Moreover, AFM can investigate samples in liquid which provides an opportunity to monitor samples close to their native surroundings. Further, AFM provides true 3D images, whereas only limited ranges in heights can be ''in-focus'' at any one time with optical and electron microscopies. Therefore, AFM can provide unique insight into the structure and functional behavior of materials including food.

AFM is a versatile technique. Besides scanning the topography of a sample, it can also be used to investigate the mechanical properties of the sample as well as the interactions between the tip and the sample. In the past two decades, AFM has been successfully applied in widespread branches of science and technology such as nanofabrication (Simeone *et al.*, 2009; Tseng *et al.*, 2008), material science (Bhushan *et al.*, 2008; Withers and Aston, 2006), and microbiology (Dufrene, 2008b; Liu and Wang, 2010; Muller *et al.*, 2009). AFM was introduced in food research in the early 1990s (Belton, 1993). Since then, AFM, as a powerful nanotechnology tool, has been extensively applied in food science and technology for a wide range of purposes (Morris, 2004; Shimoni, 2008; Yang *et al.*, 2007a).

II. PRINCIPLES OF AFM

The basic idea of AFM is to use a sharp tip scanning over the surface of a sample while sensing the interaction between the tip and the sample (Dufrene, 2008b). The tip with a flexible cantilever (in some AFM models: the sample) is mounted on a piezoelectric scanner which can move

precisely in three dimensions. During the test, a laser diode emits a laser beam onto the back of the cantilever over the tip. As the cantilever deflects under the load, the angular deflection of the reflected laser beam is detected by a position-sensitive photodiode. The magnitude of the beam deflection changes in response to the interaction force between the tip and the sample. The AFM system senses these changes in position and can map surface topography or monitor the interaction force between the tip and the sample. As the tip may collide with the surface if it is scanned at a constant height, a feedback mechanism is employed in most cases to adjust the tip-to-sample distance to maintain a constant force between the tip and the sample during the test (Fig. 6.1).

AFM provides two imaging modes, known as contact mode and dynamic mode, to visualize sample topography. In contact mode, the AFM tip raster scans over the sample to obtain high-resolution images (Fig. 6.2A). The tip and the sample surface essentially maintain contact during the scan. Low stiffness cantilevers are typically used to boost the deflection signal. However, the continuously direct contact between the tip and sample causes significant lateral force which can distort soft samples or even peel off samples which are not firmly absorbed on the substrate. In dynamic mode, including intermittent contact and noncontact submodes, the cantilever is oscillated near, or slightly above, its resonance frequency during the scan (Martin *et al.*, 1987; Zhong *et al.*, 1993).

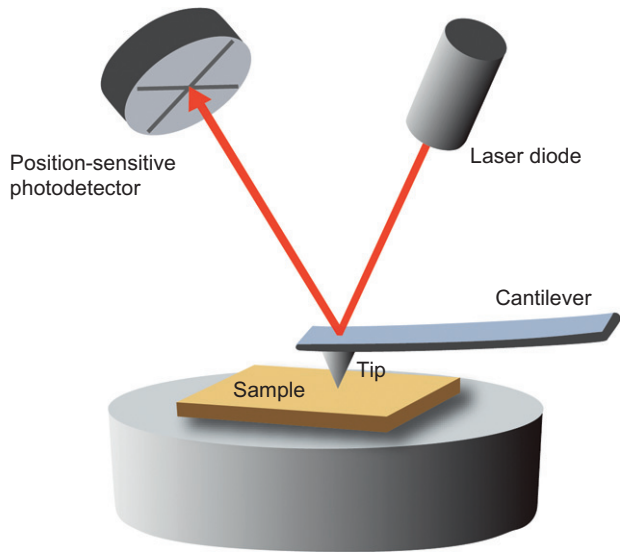

FIGURE 6.1 Diagram of AFM work principle. Reprinted with permission from Liu and Wang (2010).

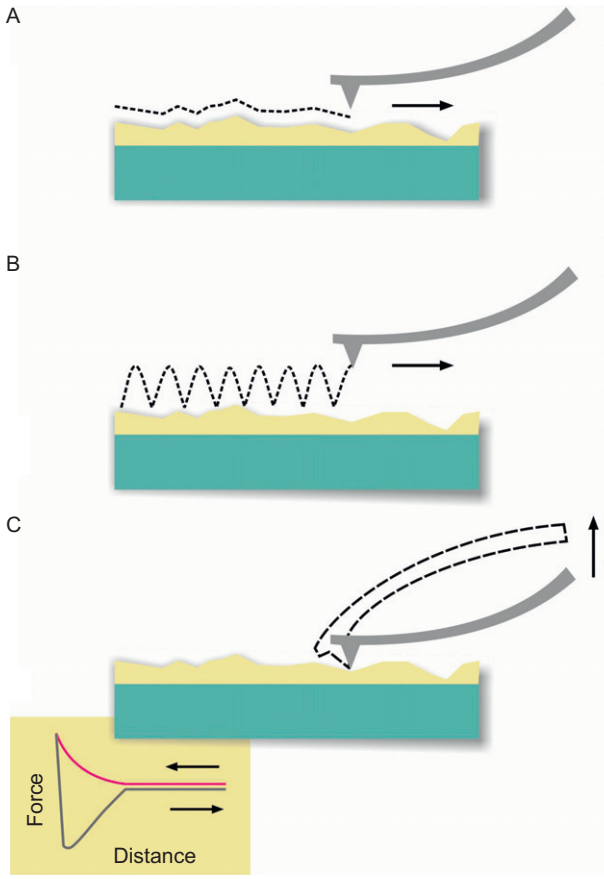

FIGURE 6.2 Diagrams of different AFM operating modes. (A) Contact mode and (B) dynamic mode for topographic imaging. (C) Force spectroscopy mode for interaction probing. Reprinted with permission from Liu and Wang (2010).

Consequently, the lateral force between the tip and sample can be significantly reduced (Fig. 6.2B). Traditionally, contact mode typically could provide higher resolution, but recent advances in noncontact techniques have led to spatial resolution up to the atomic level in vacuums and liquids (Fukuma *et al.*, 2005; Giessibl, 2003; Sugimoto *et al.*, 2007). Therefore, dynamic mode is preferred for soft and unstable samples.

The dynamic imaging mode can be further classified into two subcategories: intermittent contact mode (also known as tapping mode) and noncontact mode. In both techniques, the AFM tip is attached to the end of an oscillating cantilever. For the intermittent contact technique, the cantilever is vibrated near its resonance frequency. The amplitude of the oscillation is typically 100–200 nm with the tip intermittently contacting

the sample surface during the scan. This reduces the force exerted by the tip on the sample surfaces remarkably in comparison with the contact mode. In the noncontact mode, the cantilever is vibrated slightly above its resonance frequency with typical amplitude of several nanometers up to less than 10 nm. The tip never actually contacts the sample surface during the scan, but van der Waals forces and other long-range interactions extending above the surface influence the motion of the tip and provide information about the sample surface.

Besides topography imaging, AFM can also be used in force spectroscopy mode to measure interaction force and physical properties of samples. In this mode, the cantilever deflection (i.e., force signal) is recorded as a function of its vertical displacement (i.e., distance signal) as the tip approaches toward and retracts from the sample to obtain a force–distance curve (Fig. 6.2C). Moreover, spatial resolution can be achieved by generating a force-volume image through acquiring force–distance curves over a grid of points on the sample surface. The new frontier in this area is using specifically functionalized AFM tips to study protein unfolding/folding mechanisms and recognize molecular groups on a sample surface (Dufrene, 2008b; Muller *et al*., 2009).

Sample preparation for AFM analysis is relatively simple. Generally, a desired amount of sample is absorbed onto a smooth and clean substrate surface, for example, a freshly cleaved mica surface. For example, to prepare a food macromolecule sample for AFM imaging in air, the diluted macromolecule solution is disrupted by vortexing. Then, a small aliquot (tens of microliters) of vortexed solution is deposited onto a surface of freshly cleaved mica sheet by pipette. The mica surface is air dried before the AFM scan. A clean surrounding is required to avoid the interference of dust in the air. Molecular combing or fluid fixation may be applied to manipulate the molecule to get more information.

Modern AFM tips and cantilevers are manufactured using silicon and silicon nitride photolithographic micromachining techniques. A wide range of AFM tips with different shapes, spring constants, and resonant frequencies is commercially available (Fig. 6.3). Tips may range in size from 2 μm to tens of microns in height, with a radius of curvature as small as 2 nm. Cantilevers are usually 100–200 μm long and 0.5–2 μm thick. Their spring constants range from 0.01 to hundreds of nanonewton per nanometer. Choosing an appropriate tip will be helpful to successfully image the target sample and obtain high-resolution results. Sample characteristics, AFM test mode, and test medium will all affect the tip selection. Generally speaking, soft cantilevers are good for contact mode because they deflect without deforming the surface of the sample. Stiff cantilevers are good for dynamic mode because they have high resonant frequencies to give optimal results. During intermittent contact mode imaging, the tip will easily stick onto the sample if the force constant for

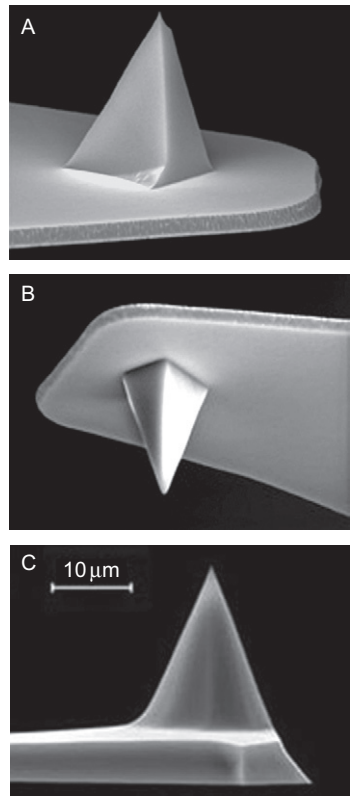

FIGURE 6.3 Images of commercial AFM tips. (A) Veeco SNL-10 (cited from http://www.veecoprobes.com/p-3693-snl-10.aspx), (B) Veeco DNP (cited from http://www.veecoprobes.com/p-3588-dnp.aspx), and (C) MikroMasch DP16/LS (cited from http://www.spmtips.com/dp/16/ls).

the tip is not large enough. The shapes of the cantilever (rectangle or triangle) typically do not have direct influence on the images.

III. REPRESENTATIVE APPLICATIONS

The most important application of AFM in food science and technology is to reveal fine structures from micrometer to nanometer level. This in depth examination of food/food component could give us a better understanding of food structure and provide clues for elucidating mechanisms of food-related phenomena. Besides image inquiring, another important application of AFM is to measure the interaction between the tip and the sample. This unique merit provides AFM the ability to analyze sample

physical properties at nanoscale. We will present several representative applications in the following sections to illustrate how to apply AFM technology in the food domain.

A. Gelatin nanostructure and elastic property

Gelatin, a water-soluble polypeptide derived from insoluble collagen, has a wide range of applications in the food industry. Most of the available gelatins are obtained from hydrolysis of mammalian collagen, usually after acid or alkaline processing. Different hydrolysis processes and biological sources could result in different gelatins. The physical properties of gelatin depend not only on the protein sequence but also on the relative contents of various collagen breakdown components and their state of aggregation. AFM is a suitable tool to reveal the gelatin structure on the nanoscale. As early as 1994, Haugstad and Gladfelter (1994) used AFM to investigate thin gelatin films deposited on mica. Two distinct film components were observed. A high-friction continuous film with thicknesses of 1–4 nm strongly adheres to mica, while a low-friction component was weakly adsorbed as large islands on top of, or small domains within, the high-friction layer. An amorphous network of fiber segments with a width of less than 10 nm and typical length of about 20–30 nm was found on the high-friction layer (Fig. 6.4). The low-friction material was interpreted as moieties of intramolecularly folded gelatin. Their thickness

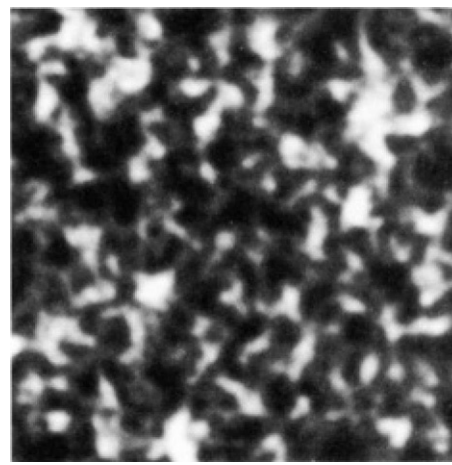

FIGURE 6.4 Small-scale topographic image (300 × 300 nm) of the high-friction layer of a gelatin film. Low-pass Fourier filtering was employed to remove most of the small wavelength noise comprising the streakiness along the fast scan axis. Reprinted with permission from Haugstad and Gladfelter (1994).

(about 1.5 nm) equaled to the diameter of the collagen-fold triple helix. Lin *et al.* (2002) investigated the effect of pH on self-association of a type-B gelatin with AFM and laser light scattering. At the isoelectric point (pH 4.94), the ampholyte gelatin macromolecules collapsed due to electrostatic attraction forces. AFM images indicated that there were both multimers and monomers. They could associate to form larger aggregates. Highly ordered aggregates were observed at higher gelatin concentration. When the pH was away from the isoelectric point, the macromolecular chains behaved like random coils. The diameters of the gelatin ''grains'' imaged with AFM were 20–50 nm with an average of ca. 40 nm, which was consistent with the laser light scattering results.

Because of safety, economic, religious, and environmental reasons, nonmammalian source gelatin is becoming more interesting in recent years. Catfish is one of the most important farm-raised fishes in the United States. Its skin is a fish processing by-product with a large annual output. Catfish skin could be a potential nonmammalian gelatin source. Yang *et al.* (2007b, 2008), Yang and Wang (2009), and Wang *et al.* (2008) investigated the gelatin extracted from catfish (*Ictalurus punctatus*) skin. AFM was used to image the nanostructures of the catfish skin gelatin obtained through an optimized two-step pretreatment extraction process (a 0.20-M NaOH pretreatment for 84 min, followed by a 0.115-M acetic acid pretreatment for 60 min at 4 °C, and then deionized water extraction for 180 min at 55 °C). The diluted and homogenized gelatin solution was applied on the mica surface and air dried before test. Most of the fish gelatin samples showed spherical structure with different diameters. The average diameter of these spherical structures was 267 ± 131 nm ranging from 89.9 to 820.4 nm, with most of them being between 160 and 280 nm (Fig. 6.5A and B). This is similar to the sizes of gelatin nanoparticles from bovine skin and porcine skin, where the average diameter is 180 ± 42 nm (Saxena *et al.*, 2005). Cavity structures were occasionally found in the AFM images. The average diameter of these annular pores was 118 ± 14 nm (Fig. 6.5C and D). After incubating the gelatin solution at room temperature for 1 h, association of the gelatin was observed. Fibril and spherical coil structures appeared during the aggregation (Fig. 6.5E and F).

The effects of gelatin concentration on nanostructures and physical properties were investigated. Catfish gelatin samples with seven concentrations, that is, 0.05%, 0.10%, 0.25%, 0.50%, 1.00%, 3.33%, and 6.67% (w/w), were tested. The results indicated that the concentration of 1.00% was a critical point for this gelatin. When the gelatin concentration was greater than 1%, the nanostructure showed fibril structures with widths of main chains of about 2–4 μm, and the physical properties including textural properties and viscosity increased quickly with the increase of concentration (Fig. 6.6A). It indicates that high texture and

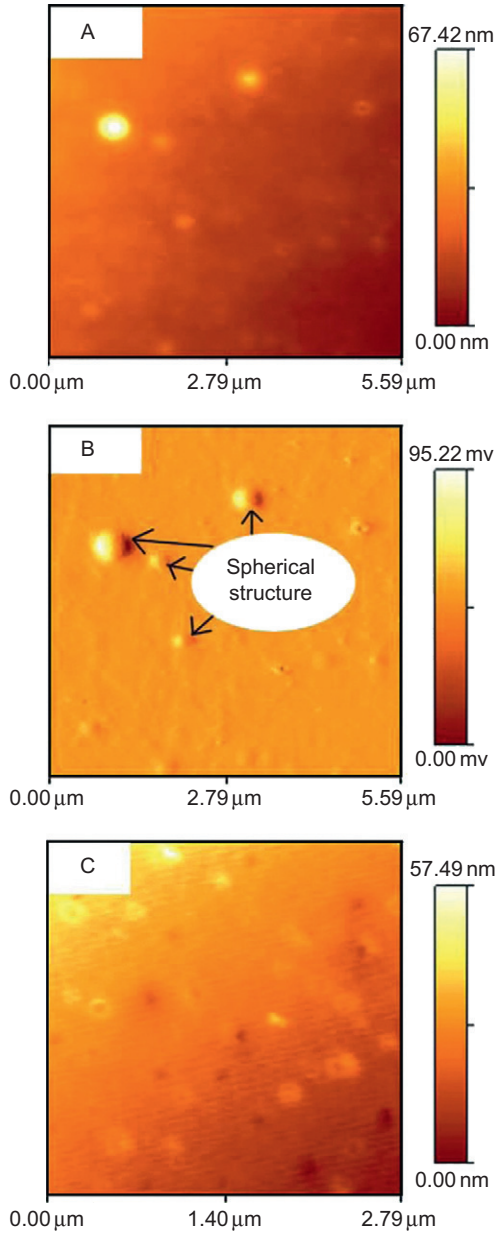

Figure 6.5 (continued)

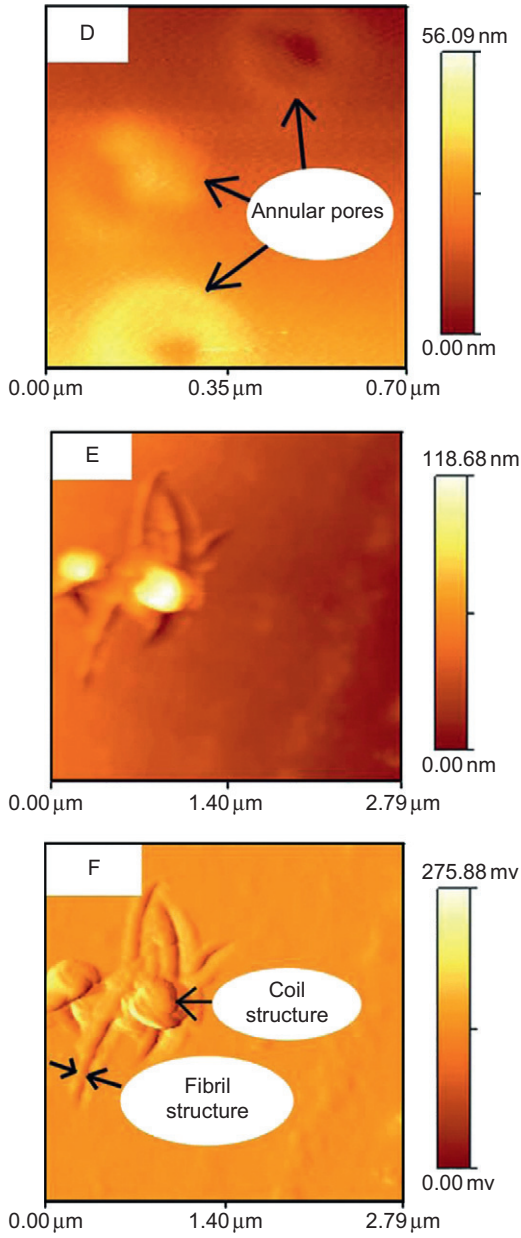

FIGURE 6.5 AFM images of catfish skin gelatin. (A) Height and (B) corresponding error-signal mode images of spherical structures; (C) and (D) height mode images of cavity structures; (E) height and (F) corresponding error-signal mode images of fibril and spherical coil structures in incubated sample. Reprinted with permission from Yang *et al.* (2007b).

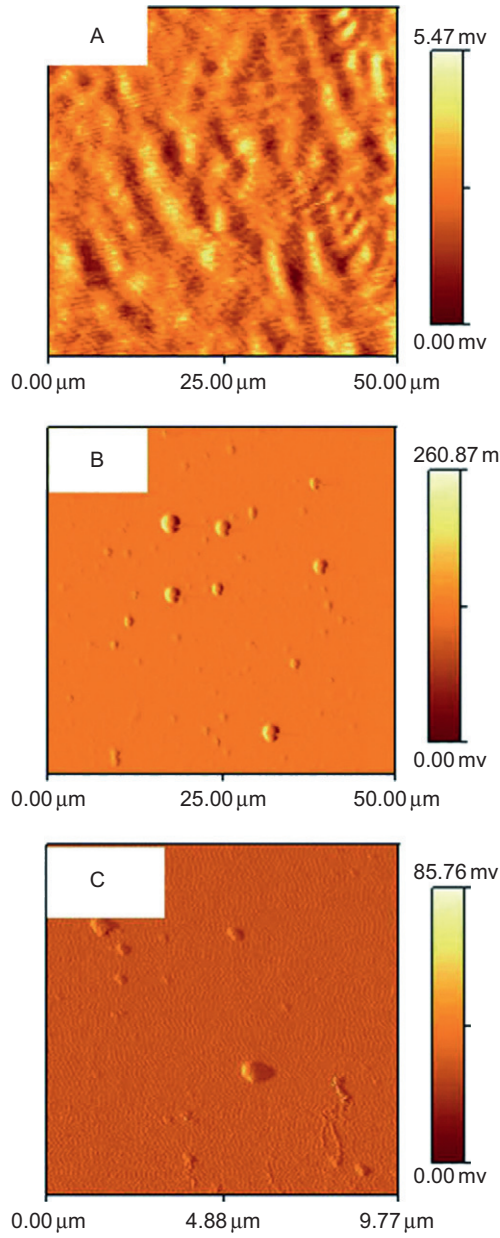

FIGURE 6.6 AFM error-signal mode images of catfish skin gelatins with different concentrations: (A) 6.67%, (B) 1.00%, and (C) 0.25%. Reprinted with permission from Yang and Wang (2009).

viscosity values might correspond to fibril nanostructures of gelatin. When the concentration was lower than 1%, the nanostructures showed mainly spherical aggregates, and the gelatin could not form the gel sufficiently to determine texture profile analysis and gel strength (Fig. 6.6C). When the concentration was 1%, the nanostructure was still mainly spherical aggregates, but it could form the gel sufficiently for texture profile and gel strength analysis (Fig. 6.6B).

To evaluate the effects of alkaline and acid pretreatment on the nanostructures and physical properties of the catfish skin gelatin, four pretreatments, that is, water, 0.1 M acetic acid, and 0.25 and 1.0 M NaOH pretreatments, were performed. The nanostructures of the resulting gelatin were then investigated. The AFM samples were prepared with diluted gelatin solutions. Gelatin obtained after water pretreatment showed large aggregates and some partially hydrolyzed segments (Fig. 6.7A and B). The relatively large aggregate of water-pretreated gelatin indicates that the gelatin is not hydrolyzed as extensively as the pretreated acid or alkaline. Gelatin obtained after acid pretreatment showed coacervates of dense matters with a large heterogeneity. There were no definite geometric structures in some parts, while fibril structures were observed in other parts (Fig. 6.7C and D). Gelatins obtained after alkaline pretreatments showed separate aggregates and annular pores (Fig. 6.7E and F). Annular pores were not observed in the water or acid pretreatment groups, suggesting that the effect only happens during alkaline pretreatment. The gelatin from alkaline pretreatment was inclined to form separate aggregates rather than continuous coacervates which were preferred by the gelatin from acid pretreatment. No evident difference was found between the nanostructures of the gelatins from the two alkaline pretreatments, indicating that the pH of the pretreatment influenced the nanostructure of the gelatin more significantly. Textural property measurements showed that the gelatin obtained after acid pretreatment had higher gel strength and hardness, which might relate to its fibril structures. No significant correlation between the aggregate diameters and the physical properties was observed.

Mechanical properties of the gel depend on many parameters, for example, gelatin source, extraction process, and gelatin concentration, and could vary in a wide range. AFM can be used to directly measure gel mechanical properties. Domke and Radmacher (1998) measured the elastic properties of thin pork skin gelatin films in water–propanol mixtures with AFM. To study the influence of the film thickness on the apparent elastic (Young's) modulus and the AFM measurement process, wedge-shaped samples with a well-defined thickness of up to 1.5 μm were prepared. Force-distance curves were collected over a grid of points on the gelatin wedge; thus, data with different film thicknesses were obtained. A steeper force curve represented a stiffer sample (Fig. 6.8).

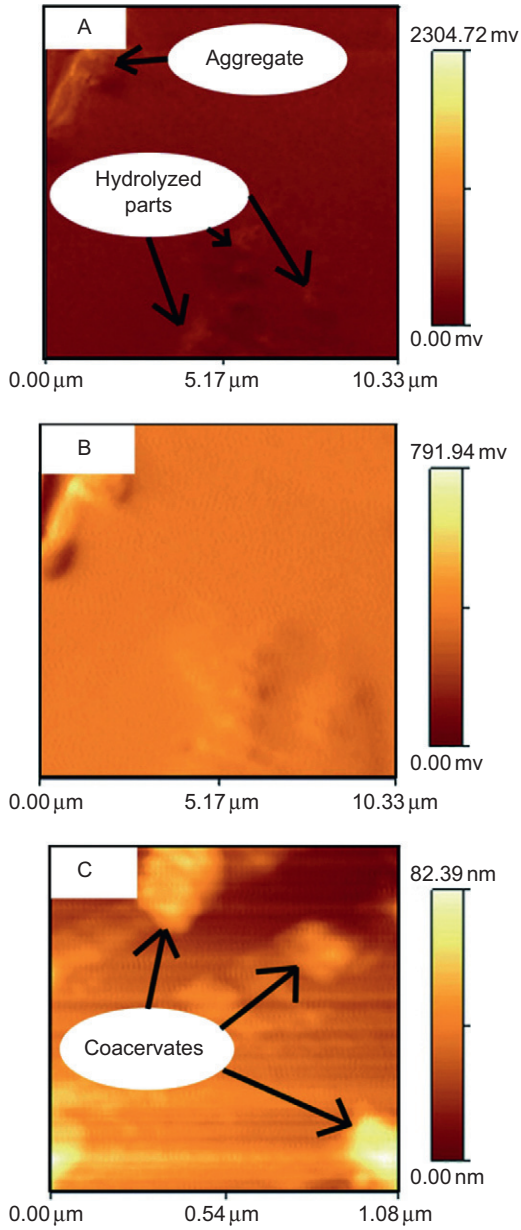

Figure 6.7 (continued)

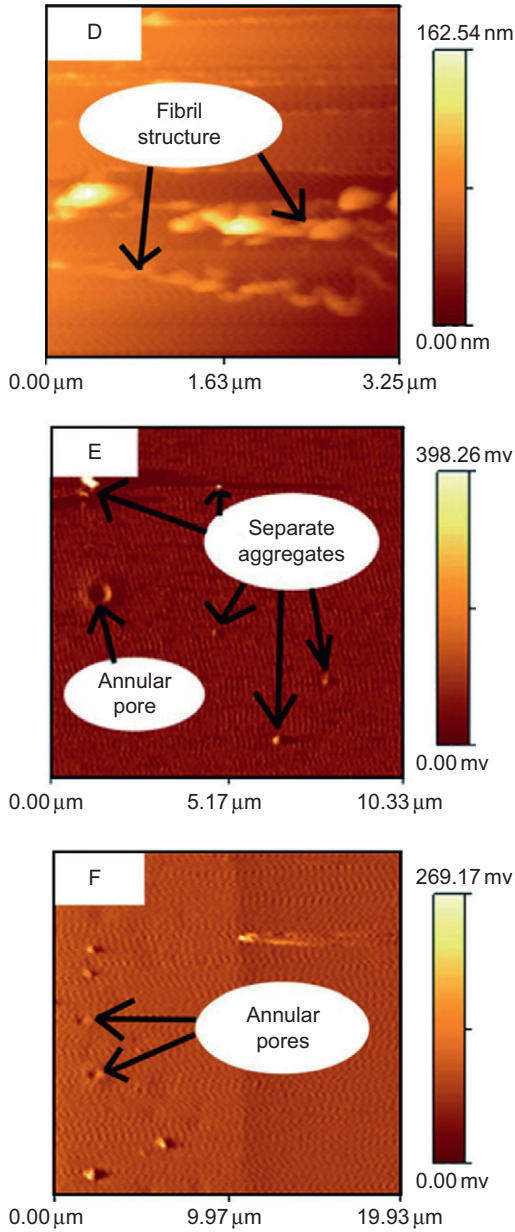

FIGURE 6.7 AFM images of catfish skin gelatin obtained after different pretreatments. (A) Phase mode and (B) corresponding error-signal mode images of gelatin obtained after water pretreatment; (C) and (D) height mode images of gelatin obtained after 0.1 M acetic acid pretreatment; (E) error-signal mode image of gelatin obtained after 0.25 M NaOH pretreatment; (F) error-signal mode image of gelatin obtained after 1.0 M NaOH pretreatment. Reprinted with permission from Yang *et al.* (2008).

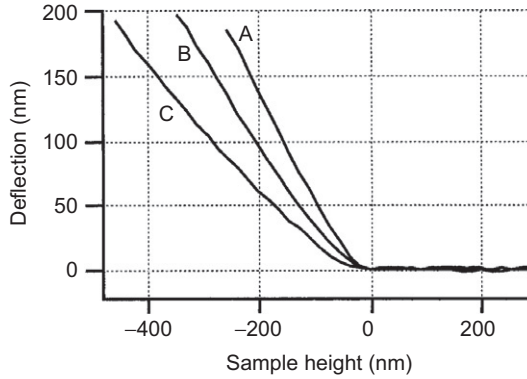

FIGURE 6.8 Three force curves taken at locations of a gelatin film thickness of 150 nm (curve A), 410 nm (curve B), and 1.15 μm (curve C). At high forces, the force curves are steeper for small thicknesses because the cantilever deflection is influenced by the underlying stiff substrate at these small film thicknesses. For comparing the slopes more easily, the curves are shifted such that their points of contact coincide. Reprinted with permission from Domke and Radmacher (1998).

The elasticity was quantitatively determined by analyzing the recorded force curves with the help of the Hertz model. The Hertz model describes the elastic deformation of two spherical surfaces touching under the load, which was calculated theoretically in 1882 by Hertz. Other effects, such as adhesion or plastic deformation, were not included in this model. Sneddon extended the calculation to other geometries. For a cone pushing onto a flat sample, the relation between the indentation δ and the loading force F can be expressed as:

$$F = \left(\frac{2}{\pi}\right)\left[\frac{E}{1-\nu^2}\right]\delta^2 \tan(\alpha) \tag{1}$$

where E is the elastic or Young's modulus, ν is the Poisson ratio of the sample, and α is the half opening angle of the indenting cone. Based on Hooke's law, the applied loading force can be calculated by:

$$F = kd = k(z - \delta) \tag{2}$$

where k is the spring constant of the AFM cantilever, d is the deflection of the cantilever, and z is the movement of the AFM piezo in z direction. Combining and transforming the former two equations yield:

$$z - z_0 = d - d_0 + \sqrt{\frac{k(d-d_0)}{(2/\pi)[E(1-\nu^2)]\tan(\alpha)}} \tag{3}$$

Then, the Young's modulus can be calculated by fitting this equation to the obtained force curve. The fitting results indicated that if the film is >1 μm and the Young's modulus is >20 kPa, the Hertz model describes the experimental data well over a wide range of loading forces; therefore, a reliable Young's modulus could be estimated. However, if the film thickness is small compared with the indentation (e.g., 120 nm), the stiff substrate influences the cantilever deflection significantly. Consequently, it is necessary to choose a small range of force curve next to the contact point to characterize the elastic properties of a thin film, and the calculated values could always represent an upper limit of the exact Young's modulus of the sample. The determined Young's modulus decreased gradually with the increase of film thickness, which could be explained by the entropic nature of rubber elasticity.

Braithwaite and Luckham (1999) studied thin layers of gelatin adsorbed on a glass sphere and a flat surface with a modified atomic force microscope. A 100-μm diameter glass bead was used to replace the traditional sharp AFM tip at the end of the cantilever. Consequently, an actual radius of curvature of the tip, which was important for modulus calculation, was obtained by sacrificing the lateral resolution of the AFM. A dynamic AFM experiment was carried out to obtain local modulus of the gelatin and the detailed mechanical properties of a solvated layer. A relatively low-frequency oscillation (20–1000 Hz) was superimposed on the linear approaching motion. The viscous and elastic properties of the gap could be determined with a separation between the modified AFM tip and the sample surface by examining the in-phase and out-of-phase responses of the AFM tip to the applied oscillation. The data indicated that a viscous response dominated until the gelatin layers interacted. After contact, the elastic response increased and dominated at a high compression of the adsorbed gelatin layers. Benmouna and Johannsmann (2004) also used a dynamic technique to investigate viscoelasticity of gelatin surfaces. A micron-sized glass sphere of 5 mm radius was attached to the AFM cantilever and used as the dynamic probe. When the sphere approaches the gelatin surface, the cantilever's Brownian movement was monitored in parallel, providing access to the dynamic sphere–surface interaction as quantified by dynamic spring constant and drag coefficient. Water–propanol mixtures were used to control the degree of swelling and thus the softness of the gelatin film. The higher the water content was, the higher degree the gelatin swelled and the softer the film was (Fig. 6.9). The results showed that there was a static repulsive force without a jump into contact during approaching. The modulus derived from the static force-distance curve was in the kilopascal range. However, the dynamic spring constant, as derived from the Brownian motion, was much larger than the static differential spring constant. On retraction, a rather strong adhesion hysteresis was observed. The strength

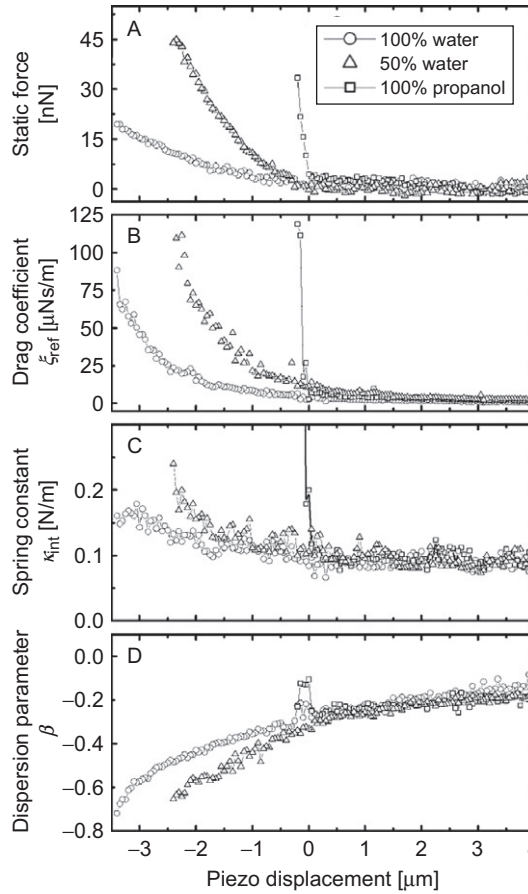

FIGURE 6.9 Dependence of viscoelastic parameters on solvent quality. The (A) static force, (B) drag coefficient at 10 kHz, (C) dynamic spring constant, and (D) dispersion parameter are shown as a function of the surface-sphere distance. The results for water, propanol, and a 50/50 water/propanol mixture are given. Reprinted with permission from Benmouna and Johannsmann (2004).

of the bridge (as given by the dynamic spring constant and the drag coefficient) was very small.

B. Casein micelle structure and nanorheology

Caseins are the major proteins in bovine milk and about 95% of the caseins exist as casein micelles. The structure and properties of casein micelles influence a wide range of technological uses of milk. Light microscopy, SEM, and TEM have been frequently used to study casein

micelles (Dalgleish *et al.*, 2004; McMahon and McManus, 1998), but their structure and stability are still not fully understood (Farrell *et al.*, 2006). Casein micelles are roughly spherical aggregates with diameters ranging from 50 to 500 nm (averaging about 150 nm) and a molecular weight from 10^6 to $>10^9$ Da (averaging about 10^8 Da) (Horne, 2009). They are composed of four different phosphoproteins: α_{S1}-, α_{S2}-, β-, and κ-caseins. The α- and β-caseins mainly make up the interior, while the surface of the micelle is rich in κ-casein. Traditionally, the C-terminal end of the κ-casein is supposed to extend into the solution and forms a so-called hairy layer. This hydrophilic layer prevents unlimited growth of the micelle by shielding further hydrophobic contacts, but this assumption has been challenged by new micrographs collected with field emission scanning electron microscopy (FESEM), which suggests a tubular surface structure extending into the interior of the micelle (Dalgleish *et al.*, 2004).

AFM has been employed to image casein micelles close to their natural condition and provide more visual information at the nanometer level. Gebhardt *et al.* (2006) investigated casein micelles and their reassociation after exposure under pressures between 0.1 and 400 MPa. Samples were set under pressure for 30 min before they were absorbed on a mica surface in a liquid cell for AFM analysis. Instead of a continuous evolution of the structure, three characteristic morphologies were observed after applying seven different pressures. The native micelles were observed after applying up to 50 MPa on the casein micelles. The micelles, with an average diameter of ca. 160 nm, appeared to be composed of elements, suggesting a rather heterogeneous morphology (Fig. 6.10A). The decomposition of the casein micelles under pressure is progressively irreversible. The casein micelles exposed to pressures between 120 and 240 MPa appeared to be compact and homogeneous. These particles exhibited little substructure. The dissociation and association processes resulted in a stable species with an average size of about 110 nm (Fig. 6.10B). When the applied pressure rose to above 280 MPa, large micelles disappeared. Particles with diameters near 20–30 nm were observed, which is consistent with the range of casein submicelles (Fig. 6.10C). Olivares *et al.* (2010) investigated casein micelles on two different substrates with AFM in air. Casein micelles were absorbed on highly ordered pyrolytic graphite (HOPG) and mica, respectively. Then they were washed with phosphate buffer, dried under nitrogen flux, and analyzed immediately. Topographical images indicated that casein micelles have spherical or pseudospherical structures with a Gaussian distribution of height counts on HOPG. The equivalent error mode signal shows that the aggregates are polydisperse in size and shape, but the submicelles with diameters of about 20 nm were not detected in this work. Significant differences in adsorption of casein micelles on HOPG and mica surfaces were observed. Casein micelles were adsorbed satisfactorily on hydrophobic HOPG, while poor

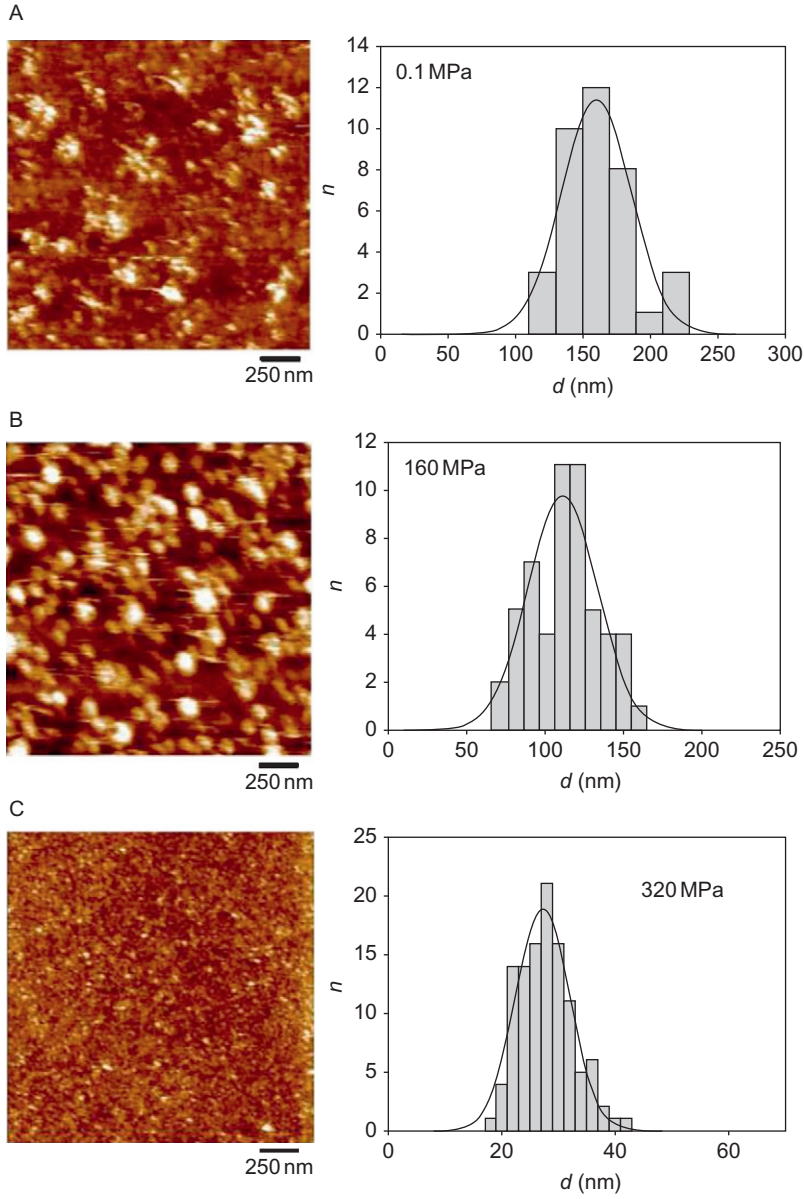

FIGURE 6.10 Three characteristic structures of pressure-treated casein micelles: representative AFM images together with the associated size-histograms are shown. The solid lines are fit to Gauss distributions. (A) Intact micelles, $P < 50$ MPa; (B) compact reconstituted micelles, 120 MPa $< P <$ 240 MPa; (C) mini-micelles, $P > 280$ MPa. Reprinted with permission from Gebhardt *et al.* (2006).

adsorption was observed on hydrophilic mica surface. Similar adsorption differences were also observed by other researchers in a liquid cell, and the adsorption of casein micelles on hydrophobic surfaces was attributed to the exposing of the hydrophobic interior of the micelle (Helstad *et al.*, 2005, 2007).

AFM was also employed to investigate casein micelles/κ-carrageenan mixture. Carrageenans are anionic polysaccharides extracted from red seaweed. When polysaccharide food gums are added to milk-based fluid systems, phase separation of casein micelles inevitably occurs, due to biopolymer incompatibility. However, a specific interaction between κ-carrageenan and casein micelles could produce a synergy which can prevent bulk phase separation, although stabilized systems are still microscopically phase separated. Milk/κ-carrageenan mixtures were analyzed by adsorbing the samples on HOPG and mica (Olivares *et al.*, 2010). It was observed that as κ-carrageenan concentration increases from 0.001% to 0.05% (w/v), the amount of casein micelles attached on HOPG surface and the heights of the micelle aggregates decreases, while an opposite absorption behavior was found on the mica surface. The amount of casein micelles and the aggregate heights both increase on the hydrophilic surface. The authors proposed a possible explanation: as hydrophilic κ-carrageenan concentration increases, it covers a greater proportion of micelle surface, increasing hydrophilic regions on the surface and leaving hydrophobic regions less available. This phenomenon confirmed that the interaction between casein micelles and κ-carrageenan may occur on the outside of the casein micelle (Spagnuolo *et al.*, 2005).

Rheological properties of casein micelle are important in milk processing. AFM provides a suitable tool to perform nanorheological measurement on single casein micelles under native conditions. Uricanu *et al.* (2004) immobilized casein micelles via carbodiimide chemistry to a self-assembled monolayer supported on gold-coated slides and studied them with a home-built AFM under serum. Force–distance curves were collected on single casein micelles. The curves in small indentation range (up to 50 nm) were fitted with the Hertz model, and the corresponding Young's moduli were calculated. The fitting results showed an elastic behavior of casein micelle for small indentations. Single casein micelles have a Young's modulus in the order of 100 kPa. The Young's modulus increased linearly with the increase of the micelle diameter. Higher temperatures and lower serum casein concentrations could result in stiffer micelles. Calcium phosphate releasing from the micelles by decreasing the pH ($\leq$5.6) did not affect the casein micelle stiffness significantly (Fig. 6.11). When the pH was below 5.0, particulate gels and multilayers were obtained. Compared to single micelles, gels from nonheated casein micelle suspensions were close to three orders of magnitude softer. Therefore, the ''softness'' of these gels did not come from the micelles

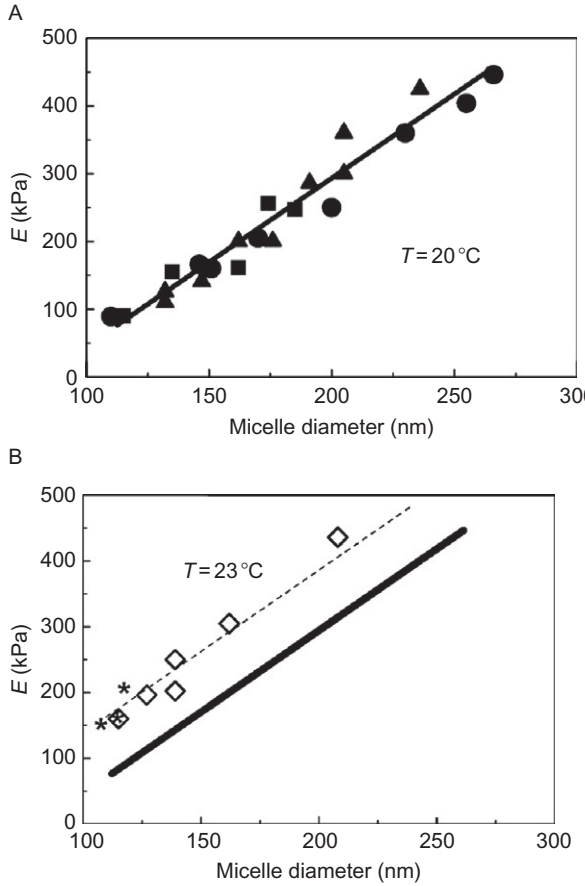

FIGURE 6.11 Young moduli (E) of casein micelles with different diameters at two temperatures: (A) 20 °C and (B) 23 °C. The data in (A) were extracted at different pH: 5.4 (squares), 5.2 (up triangles), and 5.0 (circles). For (B), besides the data from the same pH range (open diamonds), a few points (*) from pH 5.6 are included. The solid line is the best fit for the linear variation at 20 °C. Reprinted with permission from Uricanu *et al.* (2004).

themselves, indicating that flexible particle strands and/or soft intermicellar links were responsible for the gel elasticity. Helstad *et al.* (2007) further investigated the rheology of casein micelles with deep indentations. Casein micelles were adsorbed onto graphite surface under Ca–imidazole buffer at pH 7. AFM measurements in force-volume mode were performed over the total penetration depth. In the force-volume mode, force-distance curves were collected over a rectangular grid of points on the investigated surface. Then, different positions on the casein micelles

could be analyzed. The results showed that the casein aggregates were affected by the graphite surface and had a shape of a section of a spherical cap rather than a sphere. The commonly used Hertz model could not fit the experimental force–distance curves, indicating that the casein micelles could not be treated as a homogeneous elastic solid in deep indentation range. The researchers noticed that the height of the casein micelle increased linearly with its diameter, which suggested surface energy dominated liquid droplet behaviors. A surface tension-based model was then applied and successfully described many key characteristics of the nanorheological behavior of the casein micelles. The simulated force curves were in agreement with experimental findings, both with respect to slope as a function of indentation as well as describing the variation with indentation position on the micelle due to interfacial and geometric effects. An interfacial energy equivalent to 10 mJ/m^2 was estimated based on the simulation.

C. Carrageenan and gellan gum gelation mechanism and supermolecular structure

Both carrageenan and gellan gum are important polysaccharides in the food industry. They are widely used to modify food rheological and textural properties, improve moisture retention, maintain product quality during storage, and increase palatability. The gelation process is essential in their applications. Different cations could result in different aggregate structures and affect the properties of the formed gel.

Carrageenans are a family of linear sulfated polysaccharides extracted from red seaweeds. They are basically composed of a disaccharide repeating unit β-(1–3)-D-galactose and α-(1–4)-3,6-anhydro-D-galactose, in which the β-galactose is partially sulfated at the C4 position for kappa or additionally at the C2 position of the α-anhydrogalactose for iota. They can be used as a gelling agent, a water-holding agent, or a stabilizing and thickening agent in a wide range of food products (Piculell, 1995). The gelation of κ-carrageenan is believed to involve two separate and successive steps: helix formation on cooling and a further cation-dependent aggregation between helices. Ikeda *et al.* (2001) investigated gelation mechanisms of κ-carrageenan helices under different gelation conditions with AFM. Samples were prepared in aqueous solutions, spread onto freshly cleaved mica surfaces, and imaged under butanol. Imaging under a poor solvent for polysaccharides, for example, butanol, can eliminate the adhesive forces between the surface of the sample and the AFM tip. In the presence of an excessive amount of gel-promoting salt, KCl, κ-carrageenan appeared to form rigid rod-like structures considered as large aggregates of side-by-side aggregated helices. There were two types of representative structures. The first consisted of localized

networks composed of tenuous strands showing some degree of branching and with observable ends. Absence of preferential orientation suggested that the network strands were composed of aggregated helices that were rigid enough to resist being extended and, hence, oriented when spread on mica. The heights of the strands ranged between 1 and 3 nm, indicating only a low level of side-by-side association of helices. The other type of structure consisted of strands with branches and widely varying width and height (up to 6 nm). They were believed to be bundles of intensively aggregated helices. When the side-by-side interhelical aggregation was suppressed by diluting random-coiled solutions prior to cooling by adding an aggregation-impeding salt, NaI, or by transforming κ-carrageenan into the tetramethylammonium salt, κ-carrageenan helices exhibited fairly uniform strands with occasional branches and preferred orientation. However, branched rod-like structures of the carrageenan helices were still evident and the helices still appeared to be capable of associating and forming gel networks, suggesting that the side-by-side aggregation of helices is not a prerequisite for κ-carrageenan to form a network structure and the coil-helix transition itself could result in a weak and/or local network.

Funami *et al.* (2007) investigated the nanostructures of both κ- and ι-carrageenan in the presence or absence of cations and elucidated the relations between the structure and the corresponding macroscopic rheological behavior. The two types of carrageenan with equivalent average molecular weights were purified by alcohol precipitation, and subsequently transformed to the sodium type. The rheological behavior was characterized through temperature dependence of dynamic viscoelasticities in an aqueous system. ι-Carrageenan was imaged in the absence of added cation in air (Fig. 6.12A) or under butanol. The fibrils imaged in air were generally wider than those under butanol. This might be attributed to the broadening effects through a coalescence of water layer. AFM observations elucidated the difference of the effect of cations on the supermolecular structures. The presence of 0.1 M NaCl caused association within the fibrils, forming hairpins or cyclic configurations (Fig. 6.12B), and a higher concentration (0.5 M) of NaCl could cause a low level of side-by-side aggregation between helices. The presence of 0.1 M KCl resulted in the formation of strands with some degree of branching (Fig. 6.12C). The measured height was almost equivalent to that of the control on average, suggesting no inter- or intrahelical aggregation. A 0.5-M KCl could extend the strands with an increase in the stiffness. A preferential orientation was observed, but the researchers believed that it was an artifact due to the drying process in preparing the AFM sample. The presence of 0.01 M $CaCl_2$ mediated the association between the strands into network-like structures (Fig. 6.12D). This effect of $CaCl_2$ was enhanced at a higher addition level (0.05 M) making the

width of the strands and the network size larger. In summary, for ι-carrageenan, each structural change involved no or a very low level of side-by-side aggregation between helices, which was in agreement with rheological data, showing no hysteresis between sol-to-gel and gel-to-sol transitions. κ-Carrageenan was quite different. The fibrous structures of κ-carrageenan imaged in air seemed to be stiffer, showing wider variation in height or thickness in comparison with ι-carrageenan (Fig. 6.13A). The addition of 0.1 M NaCl led to the formation of longer and more extended fibrils (Fig. 6.13B), and gels were formed in the presence of 0.5 M NaCl. K^+ is the most effective cation to promote interhelical aggregation for

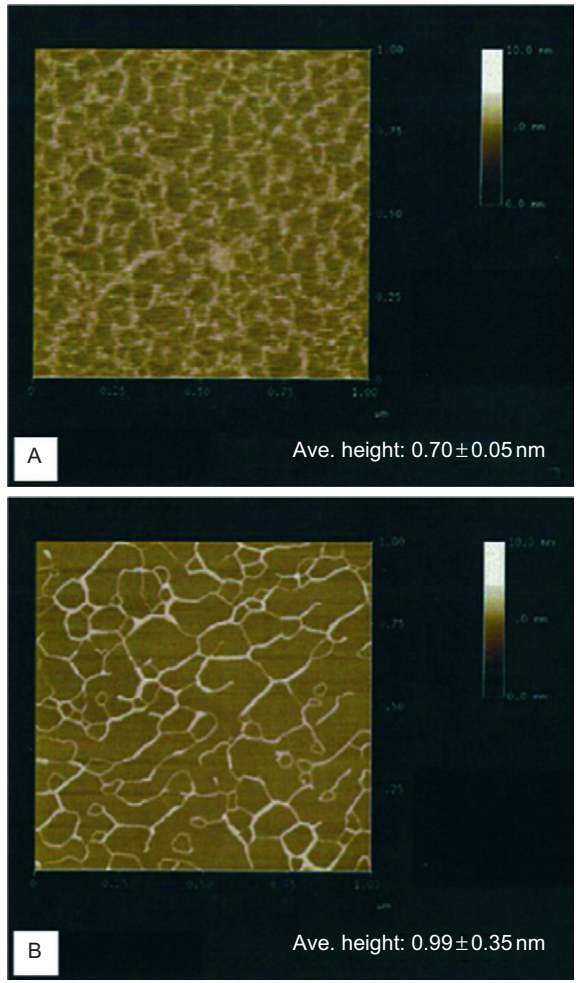

Figure 6.12 (continued)

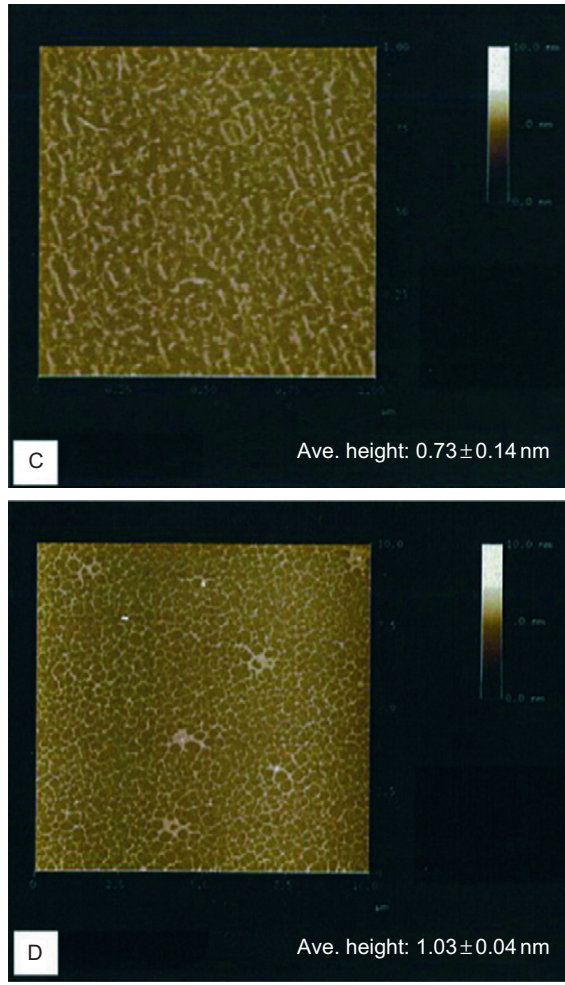

FIGURE 6.12 Topographical AFM images of ι-carrageenan obtained in air (A) in the absence of added salts, (B) in the presence of 0.1 M NaCl, (C) in the presence of 0.1 M KCl, and (D) in the presence of 0.01 M $CaCl_2$. Image size: (A)–(C), 1 × 1 μm; (D), 10 × 10 μm. Reprinted with permission from Funami *et al.* (2007).

κ-carrageenan. The addition of 0.1 M KCl formed localized network structures through a low level of interhelical aggregation, indicated by over 1 nm measured height. Different from the report of Ikeda *et al.* (2001), some degree of preferential orientation of the strands was observed (Fig. 6.13C). A higher addition level (0.5 M) of KCl resulted in larger assemblies of the molecules. An almost doubled measured height indicated side-by-side aggregation between helices. The addition of 0.01 M

$CaCl_2$ formed wide but relatively short strands without forming apparent continuous network structures in most cases (Fig. 6.13D). For ι-carrageenan, the addition of K^+ or Ca^{2+} formed localized networks through side-by-side aggregation between helices, which was consistent with the thermal hysteresis between sol-to-gel and gel-to-sol transitions. However, this interhelical aggregation was not necessarily a prerequisite for gelation.

Gellan gum is a linear, anionic heteropolysaccharide produced by a microorganism. Most applications of gellan gum are based on its outstanding gel-forming ability in the presence of certain cations at low polymer concentrations. Gellan gum can form gels with various physical

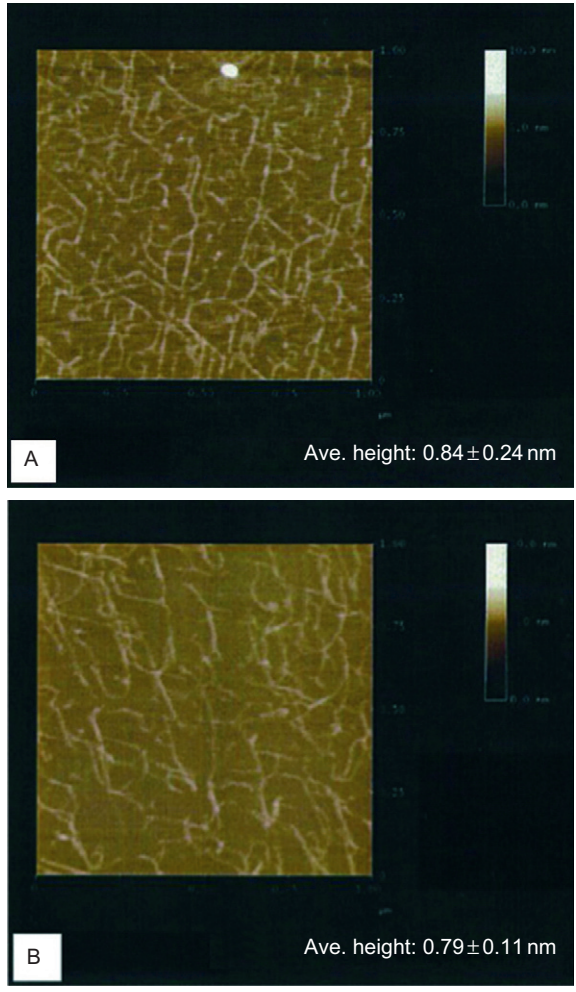

Figure 6.13 (continued)

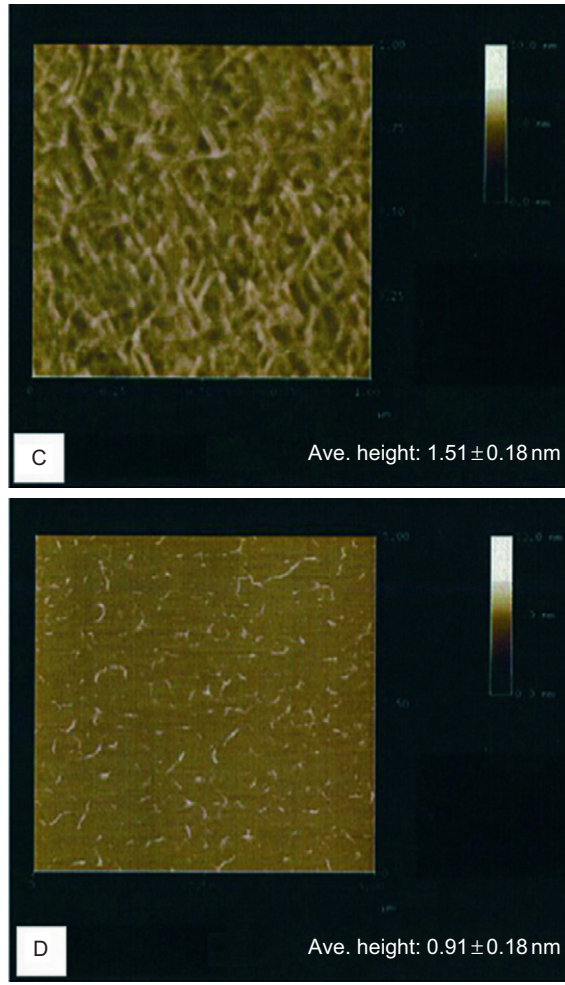

FIGURE 6.13 Topographical AFM images of κ-carrageenan obtained in air (A) in the absence of added salts, (B) in the presence of 0.1 M NaCl, (C) in the presence of 0.1 M KCl, and (D) in the presence of 0.01 M $CaCl_2$. Image size: (A)–(C), 1 × 1 μm; (D), 5 × 5 μm. Reprinted with permission from Funami *et al.* (2007).

and textural attributes depending on its acyl content and also on the types and concentrations of cations added. Noda *et al.* (2008) and Funami *et al.* (2008, 2009) used AFM to investigate the effects of different acyl contents and cations on the nanostructure of the gellan gum molecular assemblies (Fig. 6.14), and they discussed the relationships between the structures and the corresponding rheological properties. Generally, the continuousness

and homogeneity of nanostructures are related to the hysteresis and elasticity of the system, respectively. In the absence of added cations, no continuous network structure was observed regardless the acyl content of gellan

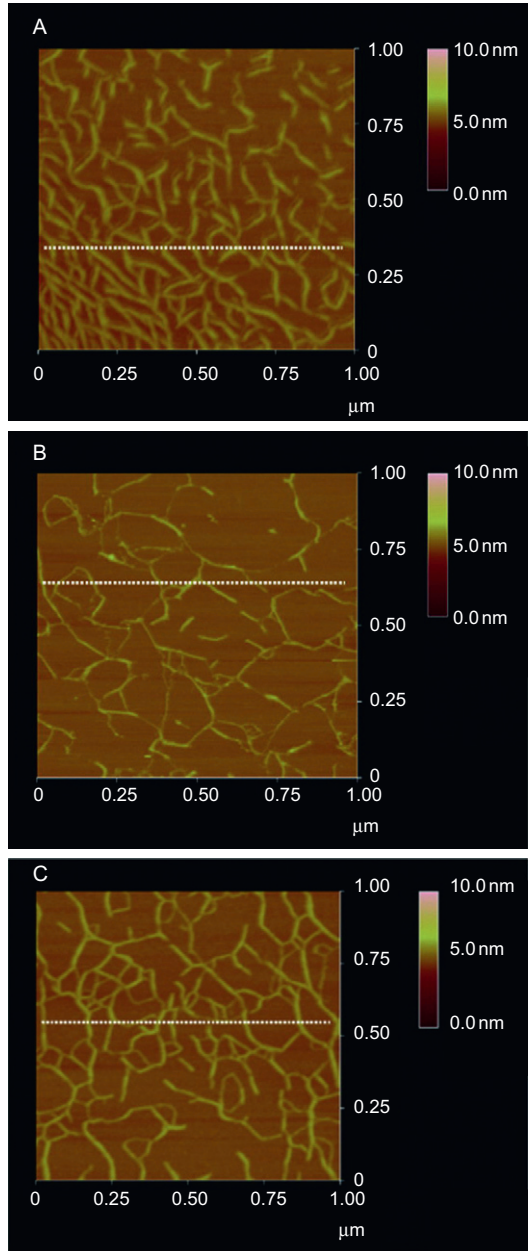

Figure 6.14 (continued)

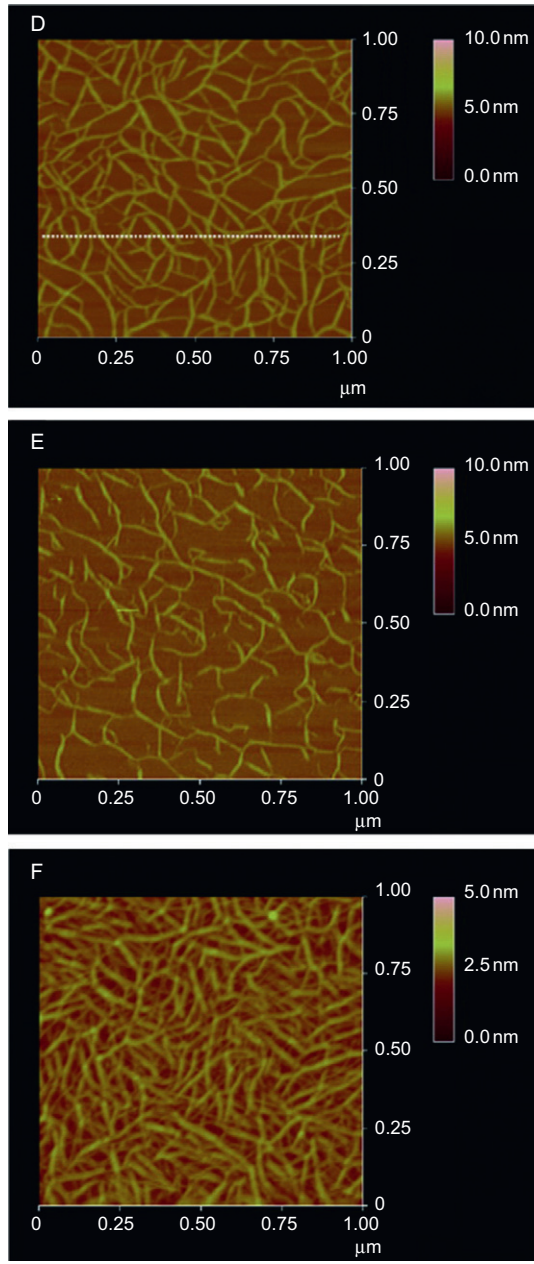

FIGURE 6.14 Topographical AFM images of molecular assemblies of gellan gum with different acyl contents in the absence of added cations (A, B) or in the presence of potassium (C, D) or sodium (E, F) cations. Acyl content—(A), (C), and (E): 13.0%; (B), (D), and (F): 8.1%. Average vertical heights on the images (A)–(F) are 0.95 ± 0.16 nm (16.8%), 0.92 ± 0.20 nm (21.7%), 1.03 ± 0.15 nm (14.6%), 1.09 ± 0.10 nm (9.2%), 1.02 ± 0.21 nm (20.4%), and 0.93 ± 0.22 nm (23.9%), respectively. Reprinted with permission from Noda *et al.* (2008) and Funami *et al.* (2009).

gum; however, the ends of the branched chains were observable, indicating that end-to-end type intermolecular associations occurred. The gellan gum with lower acyl contents exhibited more heterogeneous molecular structures. The rheological measurement showed no detectable thermal hysteresis during the conformational change from coil to helix and the subsequent intermolecular associations between the helices upon cooling and heating. Greater elasticity of the system was observed under higher acyl content because glycerate increased the stability of the double helix. In the presence of potassium cation, continuous network structures were observed for the samples with acyl contents lower than or equal to 11.9%. The continuous network structures developed mainly through end-to-end type interhelical associations rather than side-by-side type ones because no significant increase of the height of the fibers was observed. The ends of the branched chains were observable for the sample with an acyl content of 13.0% but not for the other samples suggesting that end-to-end type intermolecular associations are enhanced with decreasing acyl content. In contrast to the no added cation case, the molecular bundles seemed to become more stretched and homogeneous with decreasing acyl content. There was a thermal hysteresis between the sol-to-gel and the gel-to-sol transitions in the presence of gel-promoting cations, which became more apparent with decreasing acyl content. The gel-like properties were enhanced at lower acyl contents in the presence of potassium cation. In the presence of added sodium cation, continuous fibrous network structures were observed for a low acyl content sample, which was similar to the case of potassium cation. However, the network structures were more heterogeneous than those formed with potassium cation in terms of the height distribution of molecular assemblies. Rheological thermal hysteresis between sol-gel transitions still existed, but the storage modulus of the gelled system was only about 15% of that in the case of potassium cation at 20 °C. For a high-acyl sample, no continuous network structure was detected in the presence of added sodium cation as in the case of potassium cation. The hysteresis was even less evident. These results indicated that sodium cation was a weaker gel-promoting cation than potassium cation for gellan gum. The effects of calcium cation were also investigated, and a gel-promotion ability between the potassium and sodium cations was identified.

D. Starch nanostructure and degradation mechanism

Starch is the most important polysaccharide in the human diet. It consists of two types of molecules: the linear and helical amylose and the branched amylopectin. Depending on the source, starch generally contains 20–25% amylose and 75–80% amylopectin. In contrast to the two polysaccharides mentioned in the Section **III.C, it is a major energy

source besides being used as a thickening, stiffening, or gluing agent. Therefore, instead of gelation process, researchers are more interested in starch structure and digestion/degradation mechanisms.

Dang *et al.* (2006) investigated morphological and structural features of starch from potato (*Solanum tuberosa*) and rice (*Oryza sativa*) using AFM. Starch samples were dispersed in distilled water and heated to 90 °C for 1 h. Then, the samples were further diluted with distilled water at 90 °C to μg/mL level. The solutions were cooled to about 40 °C and filtered. A 2-μL aliquot was deposited onto freshly cleaved mica and air dried at room temperature before imaging. Aggregated structures were observed as a result of retrogradation during sample preparation. Potato amylose showed overlapping rod-like structures (Fig. 6.15A). The mean length of the structures was 504 ± 225 nm with approximately 60% of the structures being between 400 and 600 nm long, and the width ranged from 120 to 135 nm. Potato amylopectin had an open, extended form with evident branches. A distance of about 1 μm was found between many of the branch points (Fig. 6.15B). However, rice starch exhibited aligned structures with a width of approximately 250 μm. Rice amylose had well-separated, unbranched structures with a mean contour length of 652 ± 270 nm and widths of 6–19 nm (Fig. 6.15C). Moreover, the degree of polymerization was estimated by assuming that gelatinized starch molecules adopt a ''V'' structure in which six glucose residues correspond to a helical period of 2.1 nm. The calculation results showed that the degrees of polymerization of amylose from potato and rice starches were 1440 and 1860, respectively.

To study the mechanisms of degradation of crystalline starch by glucoamylases, Giardina *et al.* (2001) and Morris *et al.* (2005) visualized the interaction between *Aspergillus niger* glucoamylase 1 (GA-1) and amylose at molecular resolution with AFM. An amylose/iodine/Tween 20 complex was used to prevent the aggregation of amylose chains during sample preparation so that single amylose molecules could be imaged. GA-1 has two binding sites in the starch-binding domain (SBD). The results indicated that the two sites were independent of each other for binding but needed to work together for enzyme function. When both binding sites were active (GA-1 or catalytically inactivated GA-1), a conformational change of amylose chains was induced and circular amylose complexes were observed (Fig. 6.16A). The measured heights indicated that the GA-1 or catalytically inactivated GA-1 bound along the entire amylose chains. The mean circumference of the circular complexes was half the mean contour length of the isolated amylose chains, suggesting a two-turn helical structure (Fig. 6.16B). Abolishing one binding site (mutant GA-1s) did not prevent the amylose chain binding to the other site; however, the characteristic conformation was lost, resulting in linear amylose complexes (Fig. 6.16C). The contour length measurements

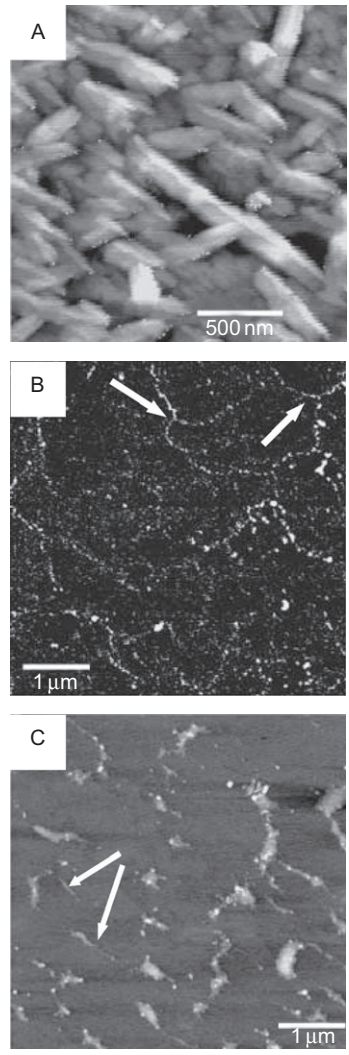

FIGURE 6.15 AFM images of (A) potato amylose, (B) potato amylopectin (arrows: branch points on the chains), and (C) rice amylose (arrows: individual amylose structures). Reprinted with permission from Dang *et al.* (2006).

suggested that the mutant GA-1s bind at the single binding site along the entire amylose chain (Fig. 6.16D). These observation results helped the researchers to propose a molecular mechanism for the role of the SBD in the hydrolytic action of glucoamylase on starch granules. The SBD first recognizes the end of amylosic double helices formed by the short amylosic chain present as branches on the amylopectin molecules and

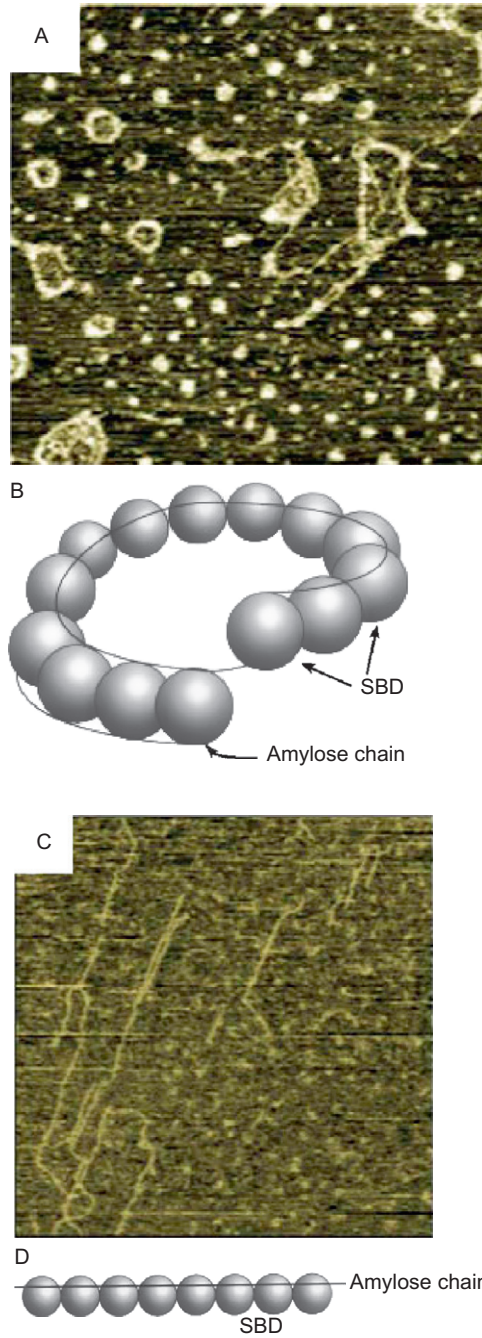

FIGURE 6.16 AFM images of glucoamylase–amylose complexes and binding models. (A) Circular amylose-GA-1 complex and (B) corresponding binding model: the balls represent starch-binding domain (SBD) and the lines represent amylose chains; (C) linear amylose–mutant GA-1 complex; and (D) corresponding binding model. Image size: $1200 \times 1200\,nm^2$. Reprinted with permission from Giardina *et al.* (2001) and Morris (2004).

displayed on the face of crystalline lamellae. Then, SBD binds at the end of the chain and distorts the structure, facilitating binding and cleavage by the exo-acting catalytic domain.

E. Interface phenomenon

Food typically is a complicated system with diverse interfaces. Stable air–water or oil–water interfaces are essential for the production of food foams and emulsions. Interface phenomena, therefore, attract great interest in the food industry. AFM provides enough resolution to visualize the interface structures, but it cannot be directly applied on air–liquid or liquid–liquid interfaces. Fortunately, the interface structure can be captured and transferred onto a freshly cleaved mica substrate using Langmuir–Blodgett techniques for AFM scan. Images are normally captured under butanol to reduce adhesion between the probe and the sample. Then, sample distortion or damage can be avoided (Morris *et al.*, 1999).

Surfactants or proteins alone can stabilize foams and emulsions, but the stability of protein-stabilized interface will be lower rather than higher when adding small amounts of surfactant. It is believed that surfactants and proteins stabilize interfaces by incompatible mechanisms. Surfactants stabilize an interface through the Gibbs–Marangoni mechanism, and this depends on rapid diffusion of surfactant molecules at the interface. However, proteins stabilize an interface by forming a strong viscoelastic network in which the protein molecules are essentially immobile. To study the unstabilizing mechanism of surfactant on a protein-stabilized interface, Mackie *et al.* (1999) used AFM to investigate the displacement of proteins from an air–water interface by surfactant Tween 20. Three different proteins, including a largely random coil protein, β-casein, and two globular proteins, β-lactoglobulin and α-lactalbumin, were tested, and protein networks were directly observed at the air–water interface. It was found that the surfactant first adsorbed at defects in the protein network. Then, these nucleated sites grew with the increase of surfactant concentration. The adsorption of surfactant into the surfactant domains reduced the local surface tension, increasing the surface pressure difference between the surfactant and protein domains and leading to the protein network compression. At sufficiently high surface pressure, the protein network failed and the proteins were released from the interface. For β-casein films, the stress propagation was homogeneous, resulting in circular surfactant domains during the replacement (Fig. 6.17A–C). However, β-lactoglobulin and α-lactalbumin formed stronger networks and the stress propagation was restricted, resulting in irregular surfactant domains (Fig. 6.17D–F). The evolution of the protein volume during the replacement process was further calculated based on protein occupied

areas and network thickness. The result showed that the volume of protein remained constant until the network failed, indicating that no protein was released from the interface until the protein network broke (Morris, 2004).

Phospholipids are amphiphilic compounds with high surface activity. They can significantly influence the physical properties of emulsions and foams used in the food industry. Rodriguez Patino *et al.* (2007) investigated structural, morphological, and surface rheology of dipalmitoylphosphatidylcholine (DPPC) and dioleoyl phosphatidylcholine (DOPC) monolayers at air–water interface. DPPC monolayers showed structural polymorphisms at the air–water interface as a function of surface pressure and the pH of the aqueous phase (Fig. 6.18). DOPC monolayers showed a

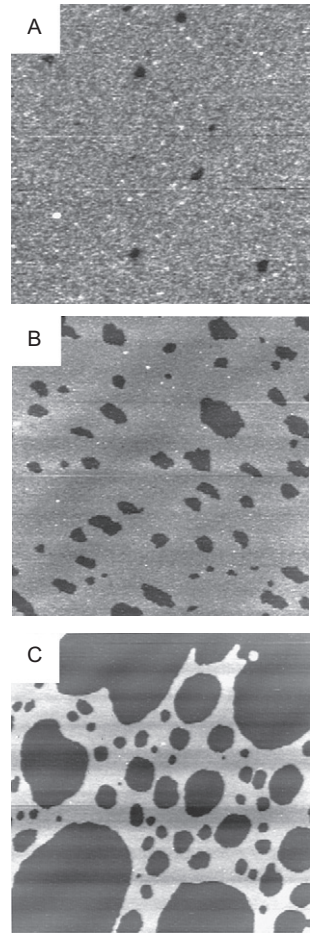

Figure 6.17 (continued)

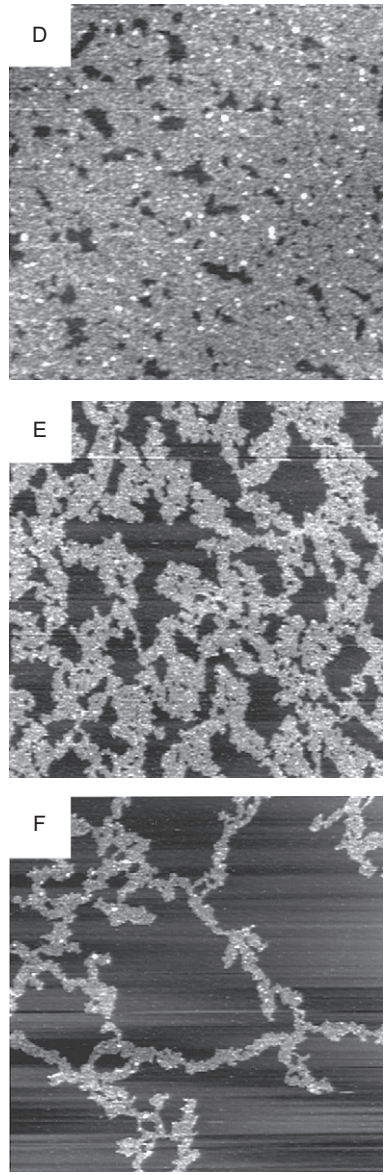

FIGURE 6.17 AFM images of the displacement processes of spread β-casein (A–C) and β-lactoglobulin (D–F) protein films from air–water interface by progressively adding surfactant Tween 20. Image size: (A) 1.6 × 1.6 μm^2, (B) 6.4 × 6.4 μm^2, (C) 6.4 × 6.4 μm^2, (D) 1.0 × 1.0 μm^2, (E) 3.2 × 3.2 μm^2, (F) 6.0 × 6.0μm^2. Reprinted with permission from Mackie *et al.* (1999).

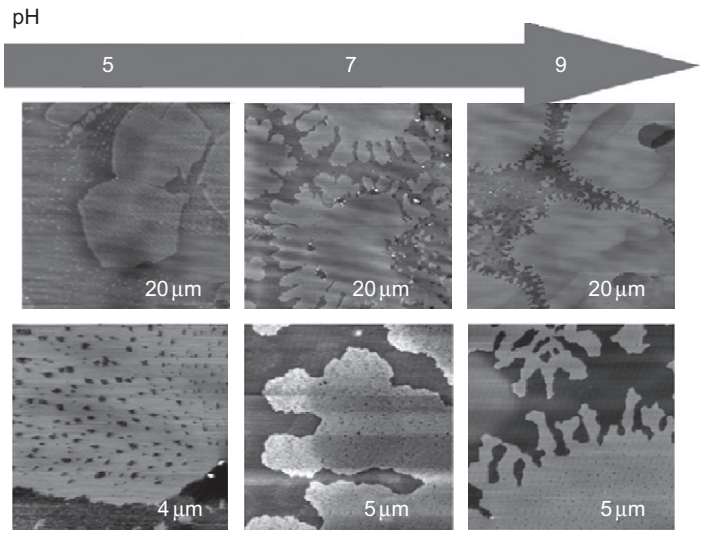

FIGURE 6.18 AFM images of DPPC monolayer structures formed at air–water interface at a temperature of 20 °C and a surface pressure of 7 mN/m. Images were collected under three different pH levels. The total image size is shown on the images. Reprinted with permission from Rodriguez Patino *et al.* (2007).

homogeneous morphology at the microscopic level; however, the nanoscopic level heterogeneity was revealed by AFM. It is observed that the relative monolayer thickness increased with surface pressure and reached a maximum at the collapse point. This confirmed that the interfacial rheology characteristics are very dependent on the structural characteristics and morphology of the phospholipids monolayers.

IV. CONCLUSIONS

AFM has been proved to be a powerful tool for morphology and rheology studies in food, providing unique insights into structures and functional behaviors on the nanoscale. It is widely applied in fundamental researches of basic food components as well as complicated food systems. Structures of molecules and their aggregates, local rheological properties, and functional mechanisms are revealed. With the help of other macroscale analysis techniques, researchers could correlate the nanoscale structures observed with AFM to the bulk properties of the food. New knowledge brought by AFM gives us a better understanding of food which can be used to improve processing and storage techniques in the food industry. In the future, AFM will continuously play an important

role in food research, and the abovementioned analytical techniques will be applied in more fields. With improvements in the instrument, researchers will be able to investigate a wider range of samples closer to their native status. Combinations with other complementary analysis techniques may provide more comprehensive information of the research object. AFM will always provide opportunities for food researchers to discover a vivid world on the nanoscale.

REFERENCES

Belton, P. S. (1993). New methods for monitoring changes in proteins. *Food Rev. Int.* **9**, 551–573.

Benmouna, F. and Johannsmann, D. (2004). Viscoelasticity of gelatin surfaces probed by AFM noise analysis. *Langmuir* **20**, 188–193.

Bhushan, B., Kwak, K. J., and Palacio, M. (2008). Nanotribology and nanomechanics of AFM probe-based data recording technology. *J. Phys. Condens. Matter* **20,** Article Number: 365207.

Binnig, G., Quate, C. F., and Gerber, C. H. (1986). Atomic force microscopy. *Phys. Rev. Lett.* **56**, 930–933.

Braithwaite, G. J. C. and Luckham, P. F. (1999). The simultaneous determination of the forces and viscoelastic properties of adsorbed polymer layers. *J. Colloid Interface Sci.* **218**, 97–111.

Dalgleish, D. G., Spagnuolo, P. A., and Douglas Goff, H. (2004). A possible structure of the casein micelle based on high-resolution field emission scanning electron microscopy. *Int. Dairy J.* **14**, 1025–1031.

Dang, J. M. C., Braet, F., and Copeland, L. (2006). Nanostructural analysis of starch components by atomic force microscopy. *J. Microsc.* **224**, 181–186.

Domke, J. and Radmacher, M. (1998). Measuring the elastic properties of thin polymer films with the atomic force microscope. *Langmuir* **14**, 3320–3325.

Dufrene, Y. F. (2008a). Towards nanomicrobiology using atomic force microscopy. *Nat. Rev. Microbiol.* **6**, 674–680.

Dufrene, Y. F. (2008b). AFM for nanoscale microbe analysis. *Analyst* **133**, 297–301.

Engel, A. and Muller, D. J. (2000). Observing single biomolecules at work with the atomic force microscope. *Nat. Struct. Biol.* **7**, 715–718.

Farrell, H. M., Jr., Malin, E. L., Brown, E. M., and Qi, P. X. (2006). Casein micelle structure: What can be learned from milk synthesis and structural biology? *Curr. Opin. Colloid Interface Sci.* **11**, 135–147.

Fukuma, T., Kobayashi, K., Matsushige, K., and Yamada, H. (2005). True molecular resolution in liquid by frequency-modulation atomic force microscopy. *Appl. Phys. Lett.* **86**, 193108.

Funami, T., Hiroe, M., Noda, S., Asai, I., Ikeda, S., and Nishinari, K. (2007). Influence of molecular structure imaged with atomic force microscopy on the rheological behavior of carrageenan aqueous system in the presence or absence of cations. *Food Hydrocolloids* **21**, 617–629.

Funami, T., Noda, S., Nakauma, M., Ishihara, S., Takahashi, R., Al-Assaf, S., Ikeda, S., Nishinari, K., and Phillips, G. O. (2008). Molecular structures of gellan gum imaged with atomic force microscopy in relation to the rheological behavior in aqueous systems in the presence or absence of various cations. *J. Agric. Food Chem.* **56**, 8609–8618.

Funami, T., Noda, S., Nakauma, M., Ishihara, S., Takahashi, R., Al-Assaf, S., Ikeda, S., Nishinari, K., and Phillips, G. O. (2009). Molecular structures of gellan gum imaged

with atomic force microscopy (AFM) in relation to the rheological behavior in aqueous systems in the presence of sodium chloride. *Food Hydrocolloids* **23**, 548–554.

Gebhardt, R., Doster, W., Friedrich, J., and Kulozik, U. (2006). Size distribution of pressure-decomposed casein micelles studied by dynamic light scattering and AFM. *Eur. Biophys. J. Biophys. Lett.* **35**, 503–509.

Giardina, T., Gunning, A. P., Juge, N., Faulds, C. B., Furniss, C. S. M., Svensson, B., Morris, V. J., and Williamson, G. (2001). Both binding sites of the starch-binding domain of Aspergillus niger glucoamylase are essential for inducing a conformational change in amylose. *J. Mol. Biol.* **313**, 1149–1159.

Giessibl, F. J. (2003). Advances in atomic force microscopy. *Rev. Mod. Phys.* **75**, 949–983.

Haugstad, G. and Gladfelter, W. L. (1994). Probing biopolymers with scanning force methods: Adsorption, structure, properties, and transformation of gelatin onmica. *Langmuir* **10**, 4295–4306.

Helstad, K. M., Bream, A. D., Trckova, J., Paulsson, M., and Dejmek, P. (2005). Nanoheological properties of casein. *In* ''Food Colloids: Interactions, Microstructure and Processing'', (E. Dickinson, Ed.), pp. 218–229. The Royal Society of Chemistry, Cambridge.

Helstad, K., Rayner, M., van Vliet, T., Paulsson, M., and Dejmek, P. (2007). Liquid droplet-like behaviour of whole casein aggregates adsorbed on graphite studied by nanoindentation with AFM. *Food Hydrocolloids* **21**, 726–738.

Horne, D. S. (2009). Casein micelles structure and stability. *In* ''Milk Proteins: From Expression to Food'', (A. Thompson, M. Boland, and H. Singh, Eds), pp. 133–179. Academic Press, San Diego.

Ikeda, S., Morris, V. J., and Nishinari, K. (2001). Microstructure of aggregated and nonaggregated κ-carrageenan helices visualized by atomic force microscopy. *Biomacromolecules* **2**, 1331–1337.

Lin, W., Yan, L., Mu, C., Li, W., Zhang, M., and Zhu, Q. (2002). Effect of pH on gelatin selfassociation investigated by laser light scattering and atomic force microscopy. *Polym. Int.* **51**, 233–238.

Liu, S. and Wang, Y. (2010). Application of AFM in microbiology: A review. *Scanning* **32**, 61–73.

Mackie, A. R., Gunning, A. P., Wilde, P. J., and Morris, V. J. (1999). Orogenic displacement of protein from the air/water interface by competitive adsorption. *J. Colloid Interface Sci.* **210**, 157–166.

Martin, Y., Williams, C. C., and Wickramasinghe, H. K. (1987). Atomic force microscope-force mapping and profiling on a sub 100-Å scale. *J. Appl. Phys.* **61**, 4723–4729.

McMahon, D. J. and McManus, W. R. (1998). Rethinking casein micelle structure using electron microscopy. *J. Dairy Sci.* **81**, 2985–2993.

Morris, V. J. (2004). Probing molecular interactions in foods. *Trends Food Sci. Technol.* **15**, 291–297.

Morris, V. J., Kirby, A. J., and Gunning, A. P. (1999). Atomic Force Microscopy for Biologists. Imperial College Press, London.

Morris, V. J., Gunning, A. P., Faulds, C. B., Williamson, G., and Svensson, B. (2005). AFM images of complexes between amylose and Aspergillus niger glucoamylase mutants, native, and mutant starch binding domains: A model for the action of glucoamylase. *Starch-Starke* **57**, 1–7.

Muller, D. J., Krieg, M., Alsteens, D., and Dufrene, Y. F. (2009). New frontiers in atomic force microscopy: Analyzing interactions from single-molecules to cells. *Curr. Opin. Microbiol.* **20**, 4–13.

Noda, S., Funami, T., Nakauma, M., Asai, I., Takahashi, R., Al-Assaf, S., Ikeda, S., Nishinari, K., and Phillips, G. O. (2008). Molecular structures of gellan gum imaged with atomic force microscopy in relation to the rheological behavior in aqueous systems.

1. Gellan gum with various acyl contents in the presence or absence of potassium. *Food Hydrocolloids* **22**, 1148–1159.

Olivares, M. L., Passeggi, M. C. G., Jr., Ferron, J., Zorrilla, S. E., and Rubiolo, A. C. (2010). Study of milk/κ-carrageenan mixtures by atomic force microscopy. *Food Hydrocolloids* **24**, 776–782.

Piculell, L. (1995). Chapter 8: Gelling carrageenans. *In* ''Food Polysaccharides and Their Applications'', (A. M. Stephen, Ed.), pp. 205–244. Marcel Dekker, Inc., New York.

Rodriguez Patino, J. M., Caro, A. L., Rodriguez Nino, M. R., Mackie, A. R., Gunning, A. P., and Morris, V. J. (2007). Some implications of nanoscience in food dispersion formulations containing phospholipids as emulsifiers. *Food Chem.* **102**, 532–541.

Saxena, A., Sachin, K., Bohidar, H. B., and Verma, A. K. (2005). Effect of molecular weight heterogeneity on drug encapsulation efficiency of gelatin nano-particles. *Colloids Surf. B Biointerfaces* **45**, 42–48.

Shimoni, E. (2008). Using AFM to explore food nanostructure. *Curr. Opin. Colloid Interface Sci.* **13**, 368–374.

Simeone, F. C., Albonetti, C., and Cavallini, M. (2009). Progress in micro- and nanopatterning via electrochemical lithography. *J. Phys. Chem. C* **113**, 18987–18994.

Spagnuolo, P. A., Dalgleish, D. G., Goff, H. D., and Morris, E. R. (2005). Kappa-carrageenan interactions in systems containing casein micelles and polysaccharide stabilizers. *Food Hydrocolloids* **19**, 371–377.

Sugimoto, Y., Pou, P., Abe, M., Jelinek, P., Perez, R., Morita, S., and Custance, O. (2007). Chemical identification of individual surface atoms by atomic force microscopy. *Nature* **446**, 64–67.

Tseng, A. A., Jou, S., Notargiacomo, A., and Chen, T. P. (2008). Recent developments in tip-based nanofabrication and its roadmap. *J. Nanosci. Nanotechnol.* **8**, 2167–2186.

Uricanu, V. I., Duits, M. H. G., and Mellema, J. (2004). Hierarchical networks of casein proteins: An elasticity study based on atomic force microscopy. *Langmuir* **20**, 5079–5090.

Wang, Y., Yang, H., and Regenstein, J. M. (2008). Characterization of fish gelatin at nanoscale using atomic force microscopy. *Food Biophys.* **3**, 269–272.

Withers, J. R. and Aston, D. E. (2006). Nanomechanical measurements with AFM in the elastic limit. *Adv. Colloid Interface Sci.* **120**, 57–67.

Yang, H. and Wang, Y. (2009). Effects of concentration on nanostructural images and physical properties of gelatin from channel catfish skins. *Food Hydrocolloids* **23**, 577–584.

Yang, H. S., Wang, Y. F., Lai, S. J., An, H. J., Li, Y. F., and Chen, F. S. (2007a). Application of atomic force microscopy as a nanotechnology tool in food science. *J. Food Sci.* **72**, R65–R75.

Yang, H., Wang, Y., Regenstein, J. M., and Rouse, D. B. (2007b). Nanostructural characterization of catfish skin gelatin using atomic force microscopy. *J. Food Sci.* **72**, C430–C440.

Yang, H., Wang, Y., Zhou, P., and Regenstein, J. M. (2008). Effects of alkaline and acid pretreatment on the physical properties and nanostructures of the gelatin from channel catfish skins. *Food Hydrocolloids* **22**, 1541–1550.

Zhong, Q., Inniss, D., Kjoller, K., and Elings, V. B. (1993). Fractured polymer/silica fiber surface studied by tapping mode atomic force microscopy. *Surf. Sci.* **290**, L688–L692.